Asymmetric impacts on Mars' polar vortices from an equinoctial Global Dust Storm

Asymmetric impacts on Mars' polar vortices from an equinoctial Global Dust Storm

Paul M. Streeter[1], Stephen R. Lewis[1], Manish R. Patel[1,2], James A. Holmes[1], Anna A. Fedorova[3], David. M Kass[4], and Armin Kleinböhl[4].

[1]School of Physical Sciences, The Open University, Walton Hall, Milton Keynes, UK
[2]Space Science and Technology Department, Science and Technology Facilities Council, Rutherford Appleton Laboratory, Oxfordshire, UK
[3]Space Research Institute of the Russian Academy of Sciences (IKI RAS), Moscow, Russia
[4]Jet Propulsion Laboratory, California Institute of Technology, Pasadena, California, USA

Key Points:

- The 2018 Global Dust Storm had significant and asymmetrical impacts on the morphology and intensity of Mars' two polar vortices
- The southern vortex was substantially diminished while the northern vortex remained robust, but both were reduced in ellipticity
- These vortex changes enhance transport into Mars' southern (but not northern) polar region and modify longitudinal transport patterns

Corresponding author: Paul Streeter, paul.streeter@open.ac.uk

This article has been accepted for publication and undergone full peer review but has not been through the copyediting, typesetting, pagination and proofreading process, which may lead to differences between this version and the Version of Record. Please cite this article as doi: 10.1029/2020JE006774.

Abstract

Mars possesses dynamical features called polar vortices: regions of cold, isolated air over the poles circumscribed by powerful westerly jets which can act as barriers to transport to dust, water, and chemical species. The 2018 Global Dust Storm was observed by multiple orbiters and offers a valuable opportunity to study the effects of such a storm on polar dynamics. To this end, we assimilate data from the Mars Climate Sounder and Atmospheric Chemistry Suite into a Mars Global Climate Model. We find that the storm had asymmetrical hemispherical impacts, with the northern vortex remaining relatively robust while the southern vortex was substantially diminished in its intensity. We propose that this asymmetry was due both to the storm's latitudinal extent, as it extended further south than north, and to its equinoctial timing, occurring as the southern vortex was already decaying. We show that both polar vortices, in particular the northern, were reduced in ellipticity by the storm. There was a well-correlated reduction in stationary topographic wave activity at high latitudes in both hemispheres. We demonstrate that the characteristic elliptical martian polar vortex shape is the pattern of the stationary waves, which was suppressed by the shifting of the polar jet away from regions of high mechanical forcing (north) or reduction of polar jet intensity by a reduced meridional temperature gradient (south). These asymmetric effects suggest increased transport into the southern (but not northern) polar region during Global Dust Storms at northern autumn equinox, and more longitudinally symmetric transport around both poles.

Plain Language Summary

Like Earth, Mars has regions of cold air around its winter poles. The temperature contrast creates powerful polar jets, polar vortices, which can block transport of atmospheric aerosols and chemicals. Unlike Earth, Mars regularly experiences Global Dust Storms which have enormous effects on atmospheric temperatures and winds. The most recent storm occurred at Mars' equinox and was observed by multiple spacecraft. We combined these observations with a numerical model. We find that the northern vortex remained relatively strong and coherent, while the southern was greatly disrupted, showing atmospheric warming and a diminished polar jet. This was because of the greater southward extent of the storm and its seasonal timing. Both vortices normally show a distinct elliptical shape; the storm made both vortices more longitudinally symmetrical. We link this to a corresponding decrease in the amplitude of topographic planetary-scale waves, showing that the elliptical shape is that of the planetary wave structure. These results suggest that equinoctial storms may enhance transport into the southern pole due to the diminished vortex, while the more robust northern vortex continues to act as an effective barrier. The reduced ellipticity of both vortices may also lead to more longitudinally symmetric transport into the polar regions.

1 Introduction

Mars' winter atmosphere is characterized by a polar vortex of low temperatures around the winter pole, circumscribed by a strong westerly jet (Waugh et al., 2016; Mitchell et al., 2015). These vortices are a key part of the atmospheric circulation and are heavily involved with dust and volatile transport (e.g. J. A. Holmes et al., 2017). Planetary polar vortices are a common feature of atmospheres in the Solar System, but Mars' differ from Earth's in several important respects. Among the most notable and visible is their peculiar annular structure. On Earth, the potential vorticity (a way of diagnosing the presence and strength of the polar vortex; see discussion below) of the polar vortices increases monotonically towards the pole; on Mars, there is a distinctive ring of higher potential vorticity around the pole, then a minimum over the pole itself (Waugh et al., 2016; Mitchell et al., 2015). This annular potential vorticity structure should be barotropically unstable but appears to persist over seasonal timescales; modelling indicates that Mars'

low radiative relaxation timescales can help maintain this equilibrium (Seviour et al., 2017). The current best explanation for the annular structure itself appears to be diabatic heating from CO_2 condensation over the winter pole; as the CO_2 condenses, it releases latent heat energy, warming the lower atmosphere and causing a local reduction in potential vorticity (Toigo et al., 2017; Rostami et al., 2018; Scott et al., 2020). Mars' polar vortices also show a hemispheric asymmetry, with the northern vortex being stronger in reanalyses than the southern (Mitchell et al., 2015).

Another feature of the martian polar vortices is their elliptical shape, particularly in the northern hemisphere (Waugh et al., 2016). It has been speculated by Mitchell et al. (2015) and Rostami et al. (2018) that this ellipticity could be linked to topography, something not incorporated into their simplified model of the martian circulation. This elliptical shape is only visible when averaged over time periods of 10s of sols; over smaller timescales, the polar vortex structure is less coherent and composed of smaller regions of high potential vorticity (Waugh et al., 2016). Rostami et al. (2018) attributed this to inhomogeneous deposition of condensing CO_2 ice. Meanwhile, Mitchell et al. (2015) found that the martian polar vortices are consistently centred over the pole itself at the solstices, suggesting a relatively lesser (compared to Earth) role for wave-mean flow interactions in controlling the shape of the polar vortices.

The martian polar vortices appear to have a complex relationship with atmospheric dust loading. Mitchell et al. (2015) found that in the MACDA reanalysis, there was less seasonal variability in the polar vortex structure due to planetary Rossby wave activity (and resulting sudden stratospheric warming), as there is on Earth; rather, any variability was linked to dust-induced changes to the Hadley circulation (and resulting intensified polar warming). Specifically, they investigated the effect of a regional dust storm at L_S=320° in MY 26 (a "C"-type storm; see Kass et al. (2016)), and found that it acted to shift the northern vortex towards the equator by ∼10° in latitude and weaken the vortex circulation overall. Guzewich et al. (2016) used an MGCM with an analytically prescribed dust scenario to investigate the effects of high southern hemisphere dust loading on the northern polar vortex, and vice-versa. They found that regional and Global Dust Storm (GDS) events could produce sudden transient vortex warming, disrupting the northern polar vortex for periods of up to 10s of sols, by shifting the downwelling branch of the cross-equatorial Hadley cell poleward. By contrast, the southern polar vortex was significantly more robust to high northern hemisphere dust loading. The exact relationship between the polar vortices and atmospheric dust content is an important one to understand, as it has implications for the transport of both volatiles and dust itself through the vortices (e.g. I. B. Smith et al., 2017; McCleese et al., 2017).

Previous studies have used reanalyses to investigate Mars' polar vortices, but to date have only used those which assimilate Thermal Emission Spectrometer (TES) data, namely the MACDA (Mitchell et al., 2015; Waugh et al., 2016) and EMARS (Waugh et al., 2016) reanalyses. This study assimilates Mars Climate Sounder (MCS) column dust optical depth (CDOD) products and MCS and Atmospheric Chemistry Suite (ACS) temperature retrievals. MCS CDOD products are not limited, as TES CDOD nadir measurements were, to areas with relatively warm surface temperatures (>220 K) (M. D. Smith, 2004), allowing greater coverage over the seasonal CO_2 caps and therefore more CDOD data for assimilation over these regions. This study also uses the newer 2D MCS retrievals, one goal of which are improved retrievals over the polar regions specifically (Kleinböhl et al., 2017). ACS temperature retrievals have the advantage of observing over different martian local times.

Crucially for the understanding of how large-scale dust loading affects Mars' polar dynamics, this study assimilates CDOD and temperature data from the real GDS that occurred in MY 34. The MY 34 GDS was first detected at L_S=186° and matured into a global, planet-encircling event by L_S=200°, before beginning its long decay phase around L_S=213° and returning to climatological levels around L_S=270° (Kass et al., 2019a). At

the height of the GDS, the planet-encircling dust cloud extended to approximately 45° N and 70° S, and the greatest atmospheric temperature response (at 50 Pa) was seen in the southern hemisphere, from the equator to the southern pole itself (Kass et al., 2019a). GDS in general have been found to have significant impacts on martian atmospheric dynamics (e.g. Fedorova et al., 2020; McDunn et al., 2013; Guzewich et al., 2014). The MY 34 event was observed by an unprecedented number of spacecraft, including the Mars Reconnaissance Orbiter (MRO) and the ExoMars Trace Gas Orbiter (TGO), making it an ideal candidate for using data assimilation to investigate its impacts on polar dynamics. Previously, Guzewich et al. (2016) used a prescribed dust scenario to investigate the effects of a GDS-like event at solstice. The use of a reanalysis allows the study of a realistic GDS-level dust loading closer to equinox, affording a chance to study GDS effects at a different season. This also allows comparison with a recent study on the MY 34 GDS using MCS data directly, and its findings of significant diurnal variation in southern polar vortex structure (Kleinböhl et al., 2020). Finally, this study devotes time to investigate wave-mean flow interactions, and specifically study how the horizontal structure of the polar vortices at this season might be affected by such interactions.

2 Methods

2.1 Model

The model used for this study is a Mars Global Climate Model (MGCM), a four-dimensional numerical model which exists as a collaborative effort between the Laboratoire de Météorologie Dynamique, the University of Oxford, the Open University, and the Instituto de Astrofísica de Andalucía (Forget et al., 1999). This version of the MGCM uses a spectral dynamical core to solve the equations of fluid motion, with a finite-difference scheme in the vertical dimension and a semi-Lagrangian scheme for tracer advection (Lewis et al., 2007). The MGCM advects dust by use of a two-moment scheme with a log-normal size distribution, and total CDOD is scaled at each column to match assimilated observations (Madeleine et al., 2011; Streeter, Lewis, Patel, Holmes, & Kass, 2020). The dust distribution in the vertical is allowed to evolve without constraint. Dust in the MGCM is radiatively active, using radiative properties derived from observations (Wolff et al., 2006, 2009). The MGCM radiative transfer scheme is reliable to within ∼10% error even at the very high dust loadings observed during the 2018 GDS (Toon et al., 1989; Streeter, Lewis, Patel, Holmes, & Kass, 2020).

2.2 Retrievals and data assimilation

The MGCM was run with a modified version of the Analysis Correction data assimilation scheme (Lorenc et al., 1991), tuned for use on the martian atmosphere (Lewis et al., 1997, 2007). Orbitally retrieved temperature profiles were assimilated using the method previously used in this scheme for TES (Lewis et al., 2007; J. A. Holmes et al., 2018) and MCS (J. A. Holmes et al., 2019; Steele et al., 2014) data, while CDOD derived from MCS limb dust profiles was assimilated to constrain MGCM dust columns (Lewis et al., 2007). The assimilation scheme and MGCM were the same as those used for the OpenMARS reanalysis dataset, which currently extends to MY 32 (J. Holmes et al., 2019).

The retrieved temperature profiles used were from MCS (McCleese et al., 2007) aboard MRO (Zurek & Smrekar, 2007), and from ACS (O. Korablev et al., 2018) aboard TGO. MCS temperature profiles extend to ∼85 km, with an intrinsic vertical resolution of ∼5 km (Kleinböhl et al., 2009). The sun-synchronous orbit of the Mars Reconnaissance Orbiter results in two approximately fixed local times for MCS observations, namely 0300 and 1500 at nonpolar latitudes (Zurek & Smrekar, 2007). The retrieval version used was v5.2, the latest version which incorporates two-dimensional radiative transfer to correct for lateral gradients in temperature and aerosol, resulting in improved retrievals over the

poles (Kleinböhl et al., 2017). The exception was during the period of the 2018 GDS, for which a reprocessed version (v5.3.2) was used; this reprocessed version incorporated information from extra channels on MCS (Kleinböhl et al., 2020). ACS temperatures for MY 34 were also assimilated, in the form of temperature profile retrievals from solar occultations by the NIR (near-infrared) channel, with an intrinsic vertical resolution of 1-3 km and altitude range of 0-90 km depending on the TGO orbit (Fedorova et al., 2020). NIR performed on average nine occultations per martian Sol throughout the relevant period of MY 34 (Fedorova et al., 2020). TGO's non-sun-synchronous orbit means that ACS temperatures were available at sunrise/sunset local times, near the terminator.

Assimilated CDOD data was from MCS, which does not directly measure dust columns but provides a derived column product based on extrapolation of retrieved dust profiles. As stated above, however, while the CDOD in the MGCM was given by assimilated MCS CDOD, the vertical distribution of dust in the MGCM was allowed to evolve freely without prescription. As MCS CDOD is reported at infrared wavelengths while the MGCM uses visible wavelengths for dust radiative transfer calculations, CDOD values were first converted from 21.6 μm to 670 nm via a conversion factor of 7.3 (Kleinböhl et al., 2011). Dayside equatorial CDOD values were filtered out before assimilation to avoid spuriously high values (Montabone et al., 2015), except during the period of the GDS itself (Montabone et al., 2020). As with MCS temperatures, v5.2 retrievals were used except during the GDS period, when v5.3.2 retrievals were used.

2.3 Simulations performed

A single MGCM simulation utilising data assimilation ("reanalysis") was performed covering multiple Mars Years, which included the periods L_S=200-220° for both MY 33 and MY 34. These periods were focussed on for the purposes of this article. The reanalysis assimilated MCS and ACS temperature profiles and MCS CDOD products. The MGCM was run at a spatial spectral resolution T42, corresponding to a spatial resolution of ∼3.75° (∼215 km at the equator), with 50 topography-following vertical levels with midpoints from at shallowest ∼5 m and at deepest ∼105 km above the surface. The MGCM was run without water cycle parametrizations in order to isolate the effects of dust.

For the purposes of this article, MY 33 was chosen as a non-GDS year to compare against MY 34. MY 33 was a very typical MCS year in terms of dust loading, including in the timing and magnitude of its regional "A"-, "B"-, and "C"-storms. The very average dust loading of MY 33 allows comparison between a situation of "normal" dust loading and a situation of GDS-scale dust loading. The L_S=200-220° period was focussed on as it represents the height of global, homogeneous dust loading during the GDS period in MY 34 (Kass et al., 2019b).

2.4 Potential vorticity diagnostic

A diagnostic used frequently throughout this article is Ertel potential vorticity (PV). PV is a measure of air circulation derived from the vorticity and stratification of the atmosphere, and is valuable for being conserved like a material tracer under adiabatic processes (Haynes & McIntyre, 1987), making it especially useful for the study of polar dynamics: the polar vortices can be defined as regions of high PV around the poles. PV has both dynamical components, in the vorticity of both the air mass itself and the planet, and thermodynamic elements, in the form of the potential temperature structure and static stability of the atmosphere. The PV of an air mass on an isentropic surface is conserved, and cannot be created, destroyed, or transported across isentropic surfaces (Haynes & McIntyre, 1987); therefore a large-scale local reduction in PV implies significant mixing along the isentropic surface, associated with diabatic and/or frictional processes. PV can be defined as

$$PV = -g(\xi + f)\frac{\partial \theta}{\partial p} \quad (1)$$

where g is the gravitational acceleration (3.72 m/s^2 on Mars), ξ is the relative isentropic vorticity (the relative vorticity of the air mass on that particular isentropic surface, an isentropic surface being a surface of constant potential temperature), f is the Coriolis parameter (the vorticity associated with the planetary rotation at a particular latitude), θ is the potential temperature, and p is the pressure.

PV is given as a value on a particular isentropic surface; this study uses the 300 K isentropic surface for consistency with previous studies of the martian polar atmosphere (e.g. Mitchell et al., 2015; Waugh et al., 2016). This corresponds to an approximate altitude range of 20-30 km, and when winds are presented in this article they are integrated between 20-30 km.

PV is typically positive/negative in the northern/southern hemisphere, and increases in magnitude near the poles due to the value of f. The term "magnitude" is used throughout this article for PV values, to make it clear that a larger negative PV value means a greater absolute value of PV. For simplicity, 1 "MPVU" (Mars potential vorticity unit) is defined throughout this article as 1×10^{-4} K m^2 kg^{-1} s^{-1}, or 100 PVU (a standard unit used for terrestrial studies).

3 Results

3.1 Diurnally averaged changes

This section explores the effects of the MY 34 GDS over both the north and south poles ("NP" and "SP") as averaged over all local times.

Fig. 1 shows the average structure of the NP and SP polar vortices between L_S=200-220° for MYs 33 and 34, and the difference between them. NP PV saw an overall reduction (Fig. 1.e) up to 15 MPVU, with the greatest reduction around latitudes 60-70° N, though PV actually increased slightly over the pole itself. The reduction was highly longitudinally asymmetric, with maxima in PV reduction in the eastern hemisphere at 180-90° E and -30-30° E. Despite this, the gross morphology of the NP vortex (Fig. 1.a,c) showed minor changes compared to the SP. The MY 34 vortex showed reduced ellipticity compared to MY 33, and the disappearance of a local PV minimum over the pole itself.

NP zonal winds also changed, tending to increase in the GDS case up to 20 m/s (Fig. 1.e) north of 60° N, particularly around 90-180° E, but decreasing southward of 60° N. The wind speed increases align with the PV decreases, occurring primarily in the east. In the western hemisphere there was little change except between latitudes 70-80° N, where zonal winds decreased by around 8 m/s between -120-30° E. At the lower latitudes 50-60° N, in (primarily) the eastern hemisphere, zonal wind speeds decreased up to 16 m/s, showing a poleward jet shift. The GDS-induced changes were asymmetric and made the MY 34 wind structure less elliptical than in MY 33. A strong local wind maximum up to 120 m/s in the eastern hemisphere (55° N, 60° E) in MY 33 was substantially reduced in MY 34, creating a more longitudinally symmetric jet. Despite the generally more symmetrical MY 34 wind structure, the jet appears shifted off-pole towards -30° E. Finally, the closer clustering of contours in MY 34 shows a latitudinal narrowing of the westerly jet. There was a visible anticorrelation between PV and zonal wind speeds.

SP PV also showed overall absolute reduction, up to 5 MPVU. The pattern of decrease (Fig. 1.f) correlates exactly with the MY 33 polar vortex structure (Fig. 1.b). The annular PV structure in MY 33 is both longitudinally asymmetric, weaker in the west/stronger in the east, and centred off-pole, with the central PV minimum around 80° S,-30° E. The MY 34 PV structure is far more uniform; there is still a (weaker) annular pattern, cen-

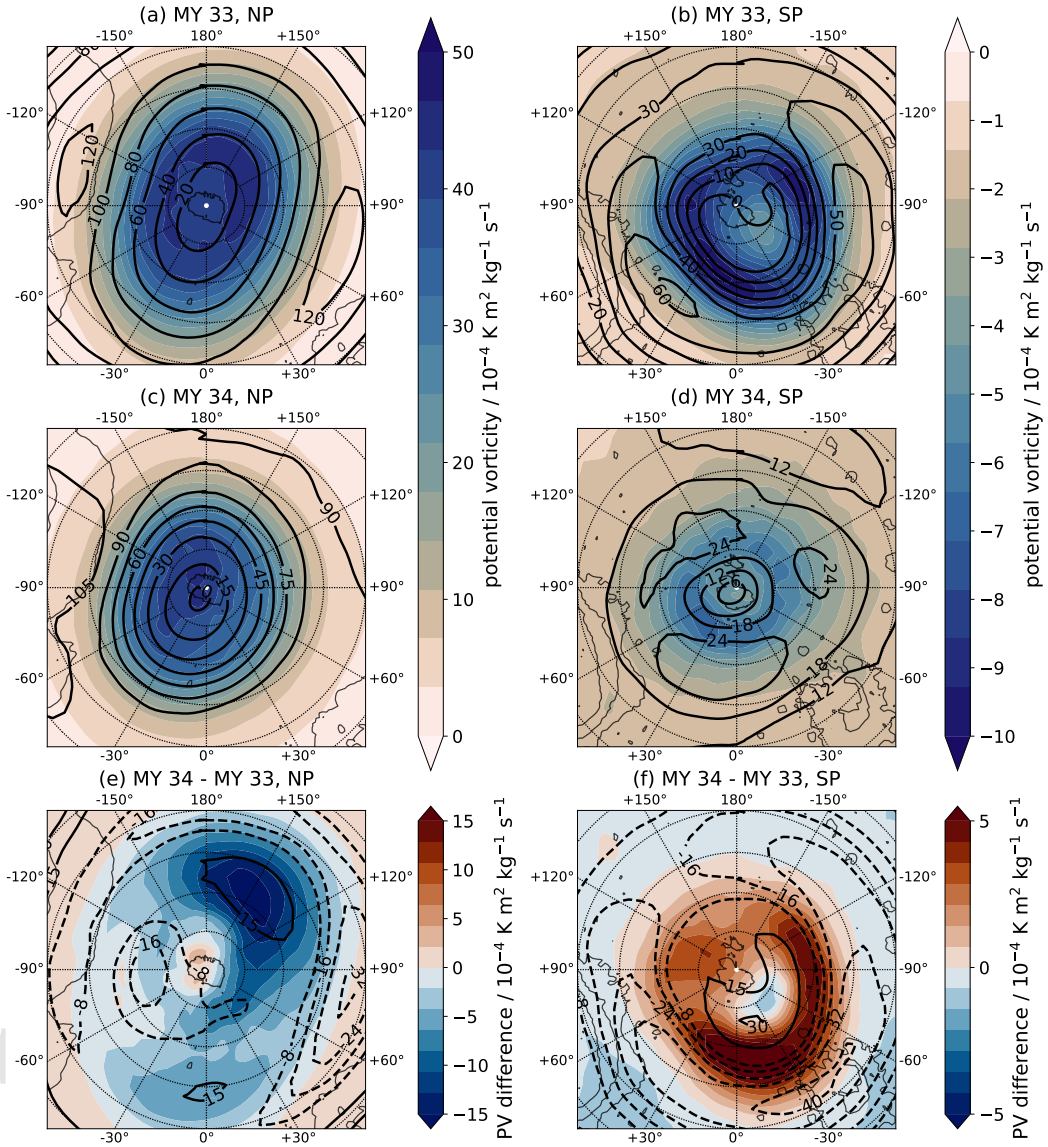

Figure 1. Potential vorticity (colours) as averaged over the L_S=200-220° period on the 300 K isentropic level (located approximately between 20-30 km altitude) and zonal wind speeds (contours) as averaged between 20-30 km for (top) MY 33, (middle) MY 34, and (bottom) the difference between MY 34 - MY 33, over the (left) north pole and (right) south pole. Plots are stereographic projections where each latitude circle is 10° separate from its neighbours and the innermost circle represents the 80° latitude band. Lower absolute values indicate lower magnitude of potential vorticity, and vice-versa. Note the difference in scales and colours. Thinner black contour lines represent surface topography.

tred over the pole itself, and reduced longitudinal asymmetry. The proportional decrease of PV at the SP (up to 50%) was much greater than at the NP, resulting in a drastically altered morphology and substantially reduced PV across the entire vortex, suggesting large-scale PV mixing from dynamical and/or diabatic changes. PV mixing is also implied by the fact that absolute PV increased slightly equatorward of 60° S.

SP zonal winds generally increased where PV decreased, up to 30 m/s, and decreased elsewhere (outside the vortex) by similar amounts (Fig. 1.f). The greatest wind increases were at the MY 33 local PV minimum (Fig. 1.b); this calm "eye" had very low wind speeds in MY 33. This signifies a shift of the remnant vortex from ∼5° off-pole to over the pole itself. Zonal wind gradients were weaker in MY 34, showing a less coherent jet core. The decrease in zonal wind speeds equatorward of 60° S was likely due to increased dust loading reducing the meridional temperature gradient. The MY 34 wind structure was more longitudinally symmetric than in MY 33, and centred around the pole itself. Again, there was a visible anticorrelation between PV and zonal wind speeds.

The MY 34 GDS significantly boosted the mean meridional circulation (MMC), strengthening both the dominant cross-equatorial clockwise and the southern anticlockwise Hadley cells (Fig. 2.I,II,III). A stronger Hadley cell signifies greater transport of (warmer) air from lower towards higher latitudes, causing adiabatic heating. The MY 34 cross-equatorial Hadley cell also extended further poleward, indicating transport towards higher northern latitudes than under non-GDS conditions; from ∼60° N in MY 33 to ∼75° N in MY 34. This was not seen in the southern anticlockwise Hadley cell.

In addition to thermally direct circulatory cells, there is frequently a thermally indirect cell at mid-high northern latitudes. Such features at mid-latitudes on Earth are called "Ferrel cells", but are not technically real circulatory cells; rather, they indicate the presence of mechanical forcing from planetary wave activity due to thermal contrasts at mid-latitudes (Salby, 2011), and their presence in the Eulerian mean meridional circulation is an artefact of the averaging process (see Andrews et al., 1987, Chapter 3). Given the thermal contrast at northern mid-latitudes at this time of year (L_S=200-220°, early northern winter) the presence of these cells implies baroclinic planetary wave activity. The weakening of the northern thermally indirect cell in MY 34 (Fig. 2) indicates that the GDS suppressed baroclinic wave activity over Mars' northern lowlands, where such activity is generally strongest (e.g. Barnes et al., 1993).

The meridional flow was altered at different longitudes, reflecting the increased longitudinal symmetry in the MY 34 polar vortex structure. Fig. 2 shows meridional winds as calculated for six different longitude ranges, at increments of 60°, which serve as a proxy for the meridional circulation at these longitude ranges. There is significant variation in the meridional flow at different longitudes.

In MY 33, the seasonally typical large-scale flow of the MMC is replicated at some longitudes: -180-120° E and 0-60° E, where the northward meridional flow extends to the NP. However, northern hemisphere southward (away from pole) flow occurs at longitudes -120-0° E and 60-180° E. These correspond to northern topographic depressions (Fig. S1) where baroclinic wave activity is strongest (e.g. Barnes et al., 1993). This pattern suggests a wavenumber 2 stationary wave. In the south, at 0-180° E (eastern hemisphere), the southward flow extends to the SP while in the western hemisphere there is northward flow, indicating wavenumber 1 stationary wave activity. These flow patterns correlate with the MY 33 polar vortex structure (Fig. 1.a,b). In both hemispheres, poleward flow correlates with where the vortex is compressed poleward, while equatorward flow correlates with where the vortex extends further equatorward.

The equivalent longitude ranges in MY 34 show complex changes, but some broad patterns are identifiable. In general, the flows show greater zonal symmetry than in MY 33, resembling the MMC more closely, especially at southern mid-high latitudes. In the

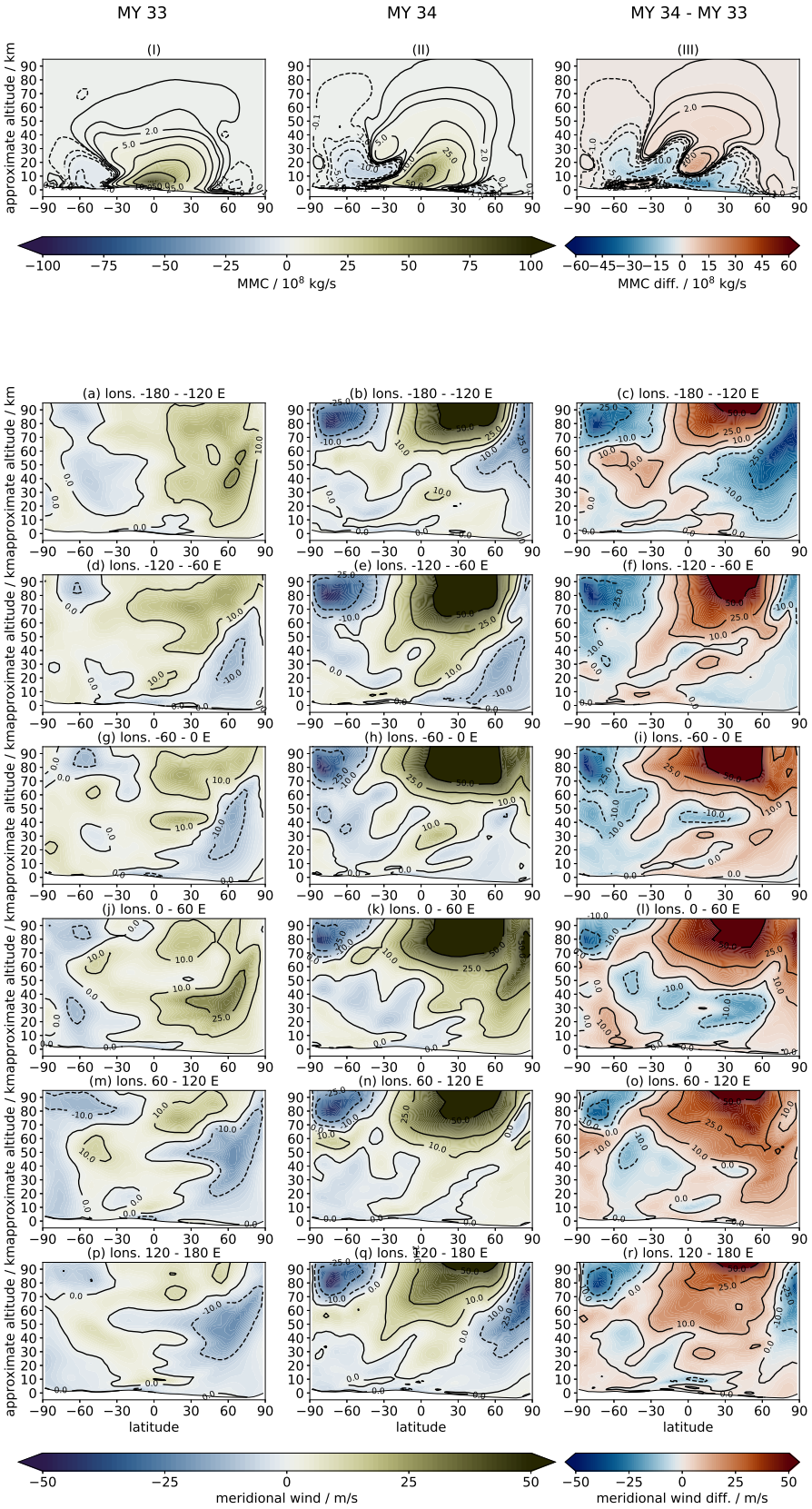

Figure 2. Top row: Mean meridional circulation calculated for the L_S=200-220° period. Positive/negative values indicate clockwise/anticlockwise flow. All other rows: meridional wind averaged over different longitude ranges for the same period. Positive/negative values indicate northward/southward flow.

north, the wavenumber 2-like pattern in MY 33 changes to a more dominant wavenumber 1-like pattern, with roughly half the planet showing northward meridional flow and half showing southward meridional flow. This generally more longitudinally symmetrical flow matches the more longitudinally symmetrical NP and SP polar vortices (Fig. 1.c,d). In the eastern hemisphere where there is southward flow extending to the SP in MY 33, in MY 34 this is significantly weakened. Likewise, in the west where there is flow away from the SP in MY 33, in MY 34 this is diminished and/or reversed. This altered flow matches the highly symmetric MY 34 SP vortex (Fig. 1.d). In the north, the MY 34 meridional flow pattern generally shows northward flow towards the NP between longitudes -60-120° E, and southward flow away from the NP between longitudes 120–-60° E. This GDS flow pattern therefore implies an MY 34 NP vortex which is compressed poleward between -60-120° E, but extends further equatorward between 120–-60° E. Examination of Fig. 1.c shows that the highest PV values can be found on the 120–-60° E side of the planet; for example, the same ∼35 MPVU contour which extends to 70° N at -150° E extends to only 80° N at 30° E.

It has been shown that the longitudinal asymmetries in the polar vortices are related to longitudinally asymmetric meridional wind patterns; but what is the cause of this longitudinal asymmetry? Fig. 3 shows the meridional wind deviation integrated between altitudes 20-30 km. The meridional wind deviation is defined as the difference between the time mean (in this case, between L_S=200-220°) of meridional wind and the time and zonal mean of meridional wind ($[v]-[\overline{v}]$, where the brackets and overbar represent time and zonal means respectively), and indicates the presence of stationary planetary waves. Fig. 3.a shows the stationary wave pattern in MY 33. A clear spatial wavenumber 2 signal is visible at northern mid-high latitudes due to the zonal topographic differences present at northern mid-high latitudes, with two notable depressions at Acidalia and Utopia plains and higher topography around Alba Patera and northern Arabia Terra (see Fig. S1), which induce differential heating and thus drive adjacent clockwise and anticlockwise circulations (Nayvelt et al., 1997; Hollingsworth & Barnes, 1996; Haberle et al., 2019). The presence of this wavenumber 2 feature and associated wind directions has been seen in observations of NP hood clouds (Haberle et al., 2019). There is a northward flow between approximately -10-70° E and 160--120° E, and a southward flow between approximately -110--10° E and 70-160° E. There is also stationary wave activity at southern high latitudes indicating a wavenumber 2 feature at mid latitudes which transitions into a wavenumber 1 feature poleward of 75-80° S; other modelling work suggests that this becomes a more unambiguous wavenumber 1 at southern winter (Hollingsworth & Barnes, 1996). There is a northward flow between approximately -70-10° E, and a southward flow between approximately 90-180° E, both extending all the way to the pole. There are also flows at southern mid-latitudes: a north-to-south flow between approximately -20-60° E, and a less well-defined south-to-north flow between approximately 60-120° E.

The MY 34 GDS drastically changed stationary wave structures (Fig. 3.b,c.); northern amplitudes were decreased up to 20 m/s. There remained two significant remnants: southward flow around -110--10° E, and adjacent northward flow around -10-70° E. These remnant flows were also constrained to poleward of ∼45° N. The other two flows were almost completely destroyed, creating a wavenumber 1-like pattern. In the south, the mid-high latitude wavenumber 2 structure was completely destroyed, leaving only a weakened wavenumber 1 feature consisting of weak northward flow between -180-60° E and weak southward flow between 60-180° E.

These stationary wave structures and changes match the polar vortex structures and changes. In the north, the MY 33 wavenumber 2 pattern matches the longitudinal asymmetry of the elliptical polar vortex (Fig. 1.a). The elongated parts of the ellipse are where the meridional wind deviation consists of southward flow, roughly between -110--10° E and 70-160° E. The narrow parts of the ellipse are where the meridional wind deviation consists of northward flow, roughly between -10-70° E and 170--110° E. The MY

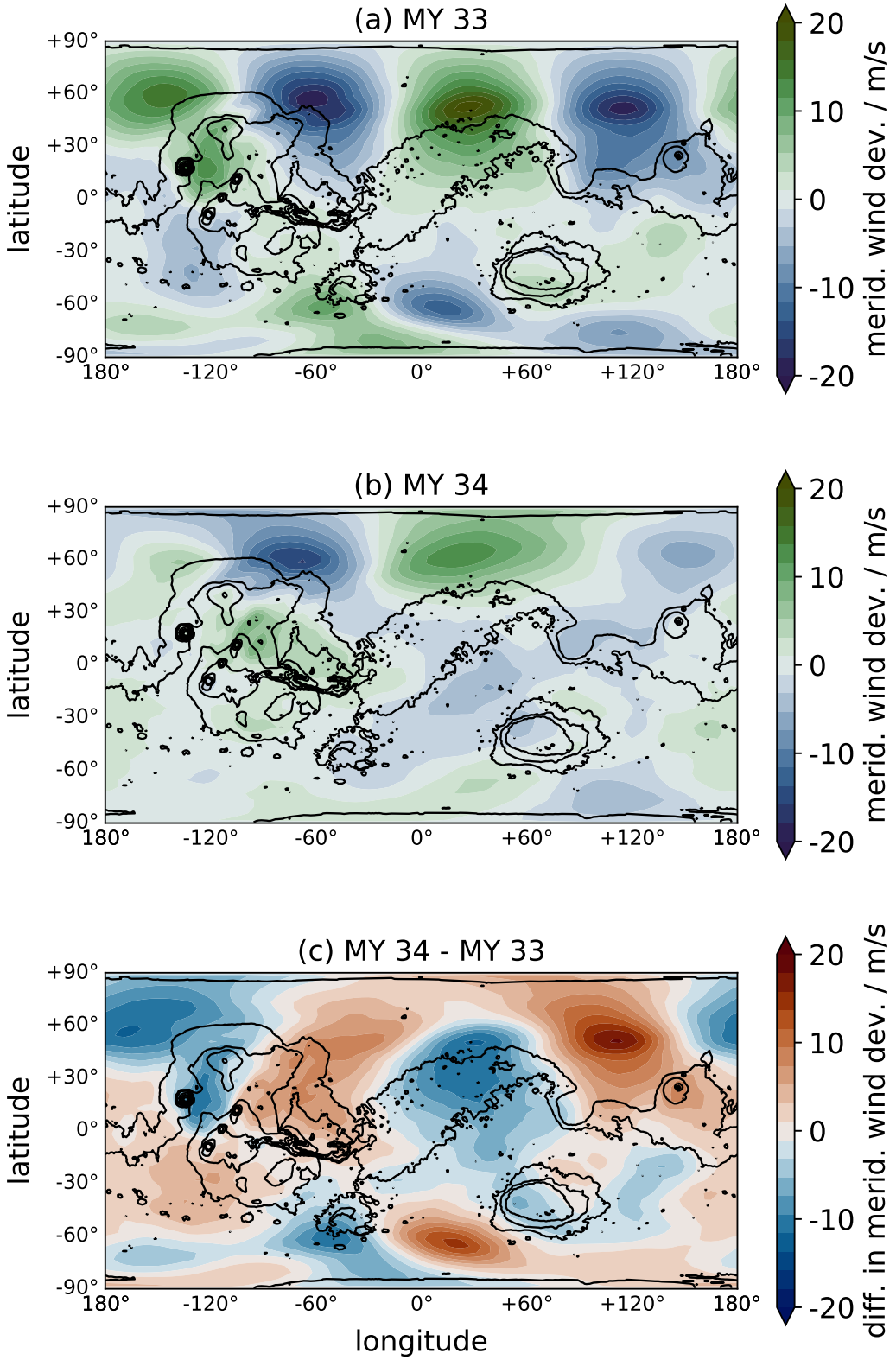

Figure 3. Meridional wind deviation ($[v] - [\overline{v}]$) at 20-30 km for L_S=200-220° for (top) MY 33, (middle) MY 34, and (bottom) the difference between MY 34 - MY 33. Red (blue) in the bottom plot corresponds to either increased (decreased) northward meridional wind deviation or decreased (increased) southward meridional wind deviation.

34 GDS significantly diminished northern stationary wave amplitudes, particularly between -180- -120° E and 70-180° E. This correlates well with the longitudes of greatest PV reduction (Fig. 1.e). Where the pre-existing stationary wave structure remained relatively intact, such as -120- -60° E, PV changes were minimal.

Likewise in the south, equatorward vortex extension matches where the meridional wind deviation consists of northward flow, between -70-10° E. Where the vortex is more constrained towards the pole is where the meridional wind deviation consists of southward flow, between 10-180° E. The MY 34 GDS almost completely destroyed southern stationary wave activity (Fig. 3.b), matching the highly symmetrical MY 34 vortex (Fig. 1.d). The greatest change occurred where the MY 33 stationary wave amplitudes were greatest, between -60-60° E; this is where the MY 33 vortex was most latitudinally extended.

While the NP PV structure was largely unaltered during the GDS except becoming more longitudinally symmetric and less annular, the SP polar vortex saw a proportionally much greater and more extensive PV reduction, even at longitudes where the stationary planetary wave pattern was not significantly altered; this suggests that in addition to dynamics, other factors contributed to the SP vortex morphological changes. Fig. 4 shows zonally averaged temperatures and dust opacities for MYs 33 and 34. It is apparent that GDS-induced atmospheric heating at southern high latitudes was much greater (up to 33 K at 20-30 km) than at northern high latitudes (up to 15 K at 20-30 km, and significantly less within the vortex). The southern diurnally-averaged vortex saw significant diminishment, while the northern diurnally-averaged polar vortex narrowed in latitudinal extent but remained coherent and clearly defined. Crucially for the SP thermal winds, the southern hemisphere meridional temperature gradient was substantially reduced except nearest the pole, visible in the increased spacing between vertical contour lines. This matches with the GDS-induced increase in dust opacity, which occurred primarily between latitudes 75° S-50° N (Fig. 4.f), though there was also a large increase (up to 0.02) between 60-90° S up to 20 km. There was little increase in dust opacity north of 60° N (<0.01), and any increase occurred below ∼10 km. This implies that diabatic heating from the increased dust presence may have had a role in affecting the SP but not NP vortex.

The plots of zonally-averaged dust opacity (Fig. 4.b,d,f) also indicate differences in tracer transport into the polar vortices from the non-GDS and GDS cases. There was a slight increase in dust opacity below 10 km around 65° N, but a slight decrease further north around 75-80° N. In the south, there was a greater dust opacity increase, up to 0.02 between 5-15 km, with smaller increases up to 30 km. This indicates minimal (if any) dust transport into the more coherent northern vortex, and possibly greater dust exclusion from the vortex itself (which could lead to increased opacities on the vortex boundary). In the south, by contrast, dust opacity increased up to 30% at around 10 km and up to 65% around 30 km (where absolute opacities are lower). The results suggest enhanced MY 34 tracer transport into the southern vortex, while the northern vortex remained a coherent transport barrier.

To better ascertain the roles of diabatic and adiabatic/dynamical heating, shortwave (SW), longwave (LW), and net (SW+LW) atmospheric radiative heating rates were calculated, and their difference between MYs 33 and 34 (Fig. 5). SW heating relies solely on the atmospheric dust presence, while LW heating is dependent on dust and atmospheric emission. Given the martian atmosphere's short radiative timescales, SW and LW heating rates should be in approximate balance in a radiative-convective model (except in the boundary layer); in a model containing dynamical processes, deviations from radiative balance indicate the presence of dynamical heating/cooling (Wolff et al., 2017). For example, in MY 33 dynamical cooling is visible between 0-60° S at 10-30 km, showing the upwelling Hadley cell branches, while dynamical heating is visible at high altitudes be-

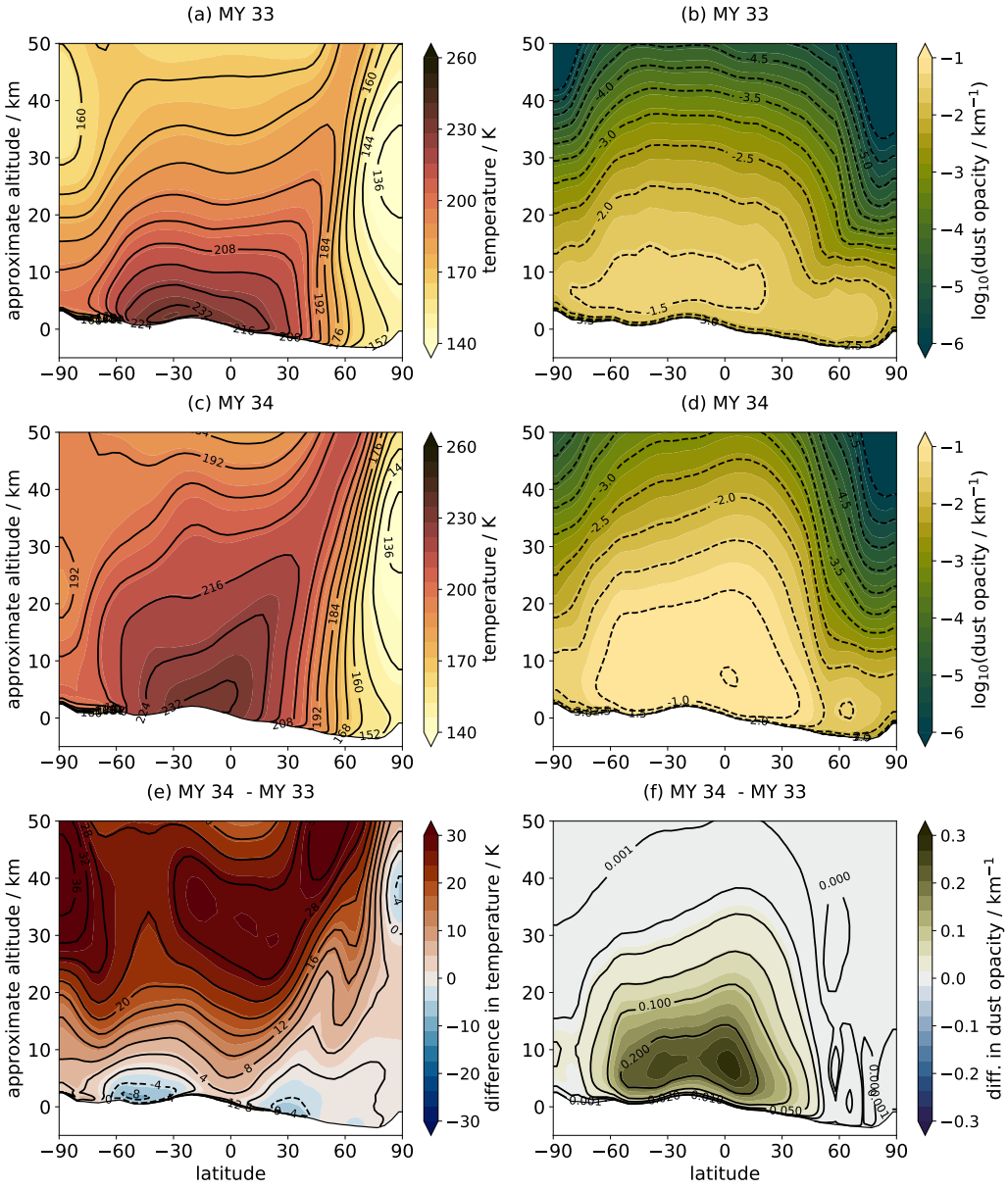

Figure 4. Zonally-averaged (left) temperatures and (right) dust opacities averaged between L_S=200-220° for (top) MY 33, (middle) MY 34, and (bottom) the difference between MY 34 - MY 33. The plotted dust opacities in subplots b. and d. are $\log_{10}$ values; those in subplot f. are actual dust opacities. All dust opacities are at 670 nm, as used in the MGCM. Altitude was cropped to 50 km for the plots.

tween 30-60° N and 60-90° S, showing the downwelling Hadley cells and Mars' characteristic polar warming (e.g. Wilson, 1997; McDunn et al., 2013).

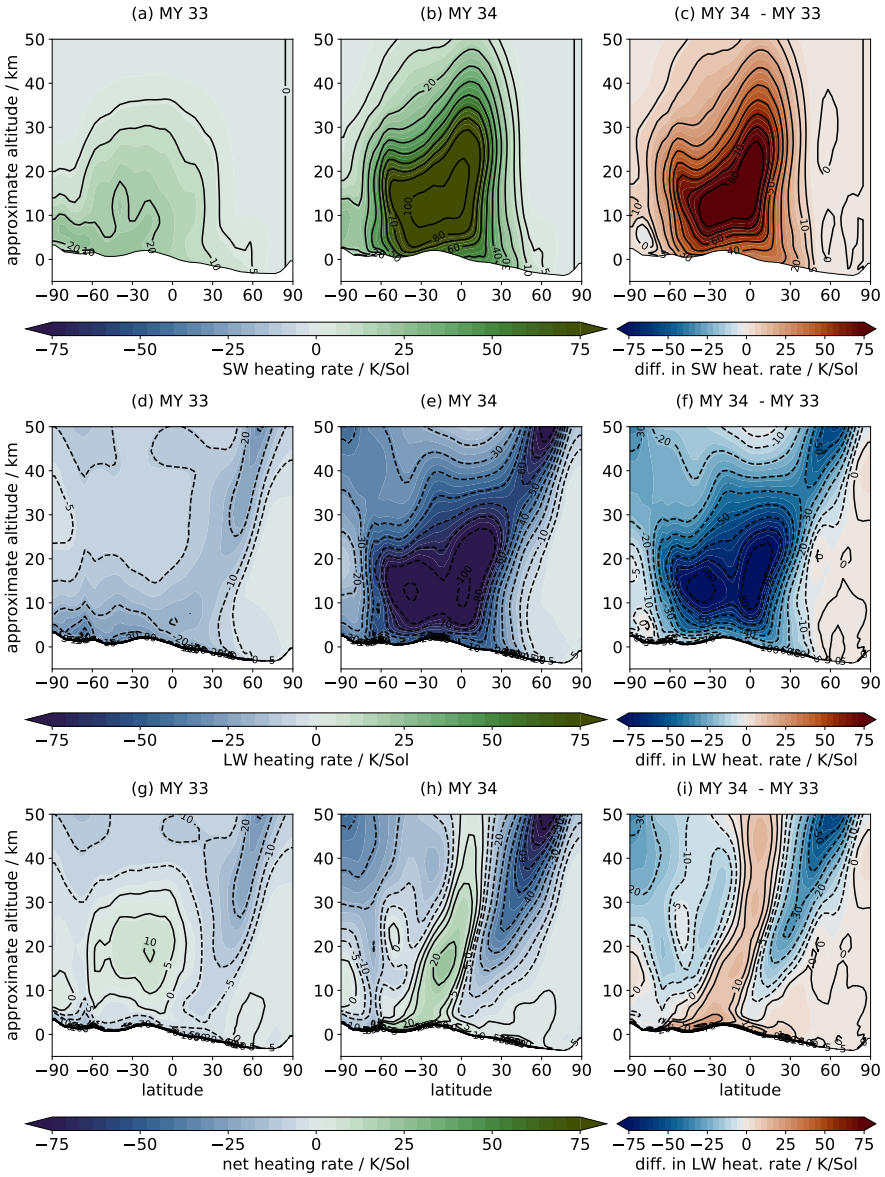

Figure 5. Zonally averaged (top) shortwave (SW), (middle) longwave (LW), and (bottom) net (SW+LW) radiative heating rates averaged between L_S=200-220° for (left) MY 33, (middle) MY 34, and (right) the difference between MY 34 - MY 33. Altitude was cropped to 50 km for the plots.

The increased dust loading in MY 34 caused increases in both SW heating and LW cooling rates, particularly between latitudes 75° S to 45° N. Southern SW heating rates

increased south to 75° S and up to 30 km altitude by at a minimum 6 K/sol (Fig. 5.c), indicating the important role of direct dust-related atmospheric heating at southern high latitudes. This heating helped reduce the meridional temperature gradient at southern high latitudes, weakening the thermal polar jet and thus reducing relative vorticity, causing local PV reduction via equation 1. This local PV reduction implies equatorward PV mixing, visible in the small absolute PV increase equatorward of 60° S (Fig. 1.f) as well as, in the presence of diabatic processes like diabatic descent, destruction of isentropic PV (Hoskins et al., 1985). PV destruction at higher latitudes has been estimated to occur on timescales of ∼5 sols around solstice (Barnes & Haberle, 1996), though this is likely shorter under significant diabatic heating (e.g. sunlight, dust diabatic heating, CO_2 condensation) and could be much longer during polar night given estimated air ages there of up to 300 sols (Waugh et al., 2019). In the north, by contrast, there was minimal alteration to SW heating rates poleward of 45° N, due to the absence of dust. Dynamical heating was also altered by the GDS: there was an increase in polar warming at both the NP and SP due to the enhanced Hadley circulation, indicated by the increase in LW cooling rates (Fig. 5.f,i). The increased dynamical heating over the SP occurred primarily above 30 km, though there was also a ∼10 K/sol increase between 20-30 km at 65° S. In the north, the increased dynamical heating narrowed the size of the polar vortex, but did not cause large-scale local PV reduction as in the south.

The results from analysis of atmospheric temperatures, dust opacities, and radiative heating rates suggest that the GDS induced significant dynamical changes at both poles, but also impacted the SP alone through increased diabatic heating. The effect in the north was to narrow the latitudinal extent of the polar vortex and make the polar vortex structure less elliptical and more longitudinally symmetric, but local PV reduction in the vortex was relatively minimal. The effect in the south, by contrast, was both to create a more symmetrical polar vortex and also to significantly reduce PV across the entire pole by reduction of the polar jet through atmospheric heating, leading to a much diminished diurnally-averaged SP vortex.

3.2 Diurnal behaviour

This section investigates how each polar vortex was affected by the GDS at different local times. As well as the NP/SP notation described above, this section also employs the concept of Mars Universal Time (MUT). MUT is the local time at longitude 0°, e.g. MUT 00:00 is when it is midnight at longitude 0°, midday at longitude 180°, etc. Note that the MGCM uses Mars hours and minutes, of which there are the same number in a martian sol as there are SI hours and minutes in a terrestrial day; seconds are SI seconds.

The SP vortex exhibited a high degree of diurnal variation. This behaviour was first noted in MCS temperature and dust extinction profile observations from MCS by Kleinböhl et al. (2020): a mass of colder, more isolated air (indicated by higher PV) and depletion of dust (indicated by lower dust amounts, in particular at higher altitudes) following the planet's nightside, centred around MUT 06:00. This is reproduced in the reanalysis (Fig. 6.g-l): the higher absolute PV mass is centred at MUT 06:00, and followed around by a corresponding CDOD minimum (<0.6). Interestingly, there does appear to also be diurnal variation in the magnitude of the high PV mass, with its absolute PV being greater at MUT 02:00 and 14:00 than at 06:00 and 18:00. This asymmetry suggests that there may still be longitudinally asymmetric processes at work, despite almost complete destruction of the southern high-latitude wavenumber 1 feature (Section 3.1).

Kleinböhl et al. (2020) attribute the diurnal behaviour of the SP vortex during the GDS to the variation of the MMC throughout the day, with the GDS-enhanced circulation amplifying a pre-existing pattern. To argue for this point, they present the MY 34 MMC as calculated for different local time ranges in an MGCM, with the spatial dust

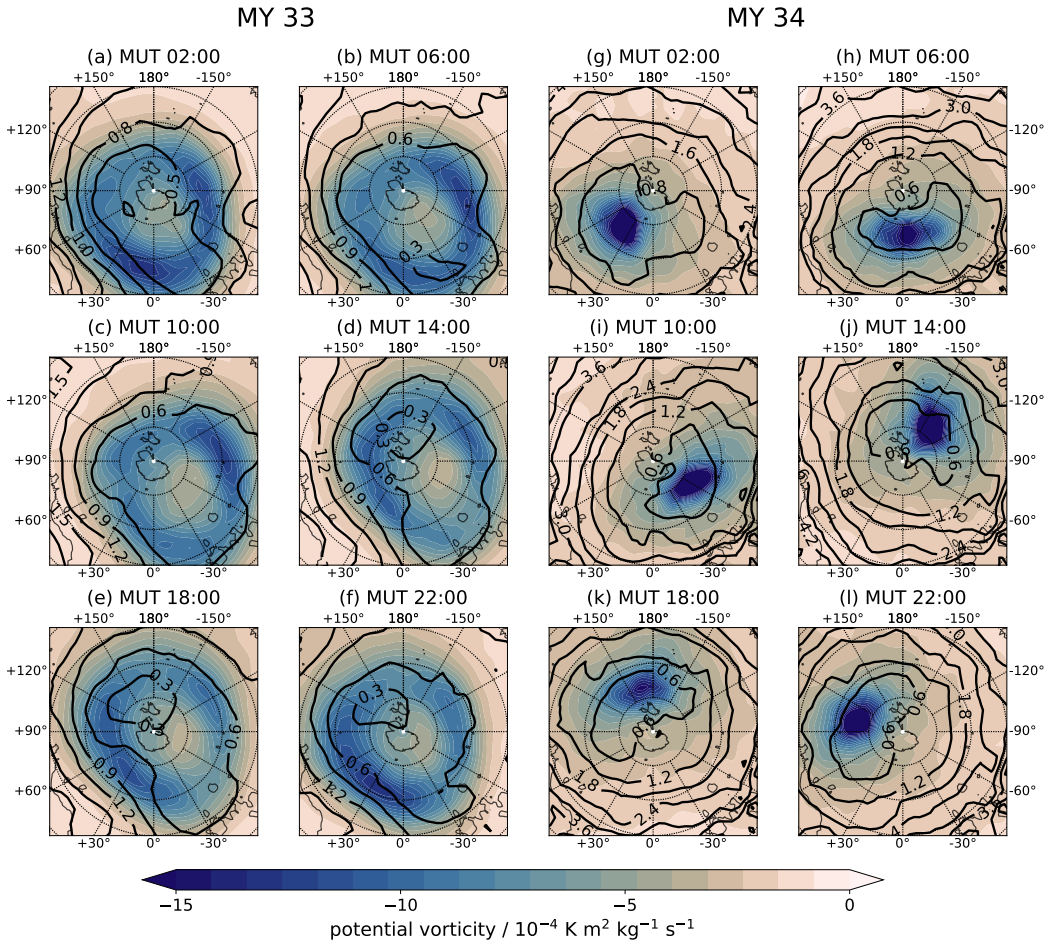

Figure 6. Potential vorticity (colours) as averaged over the L_S=200-220° period on the 300 K isentropic level and CDOD at 610 Pa (contours) over the SP for MY 33 and 34 at six different MUTs. Each MUT is averaged over the 2 hours before and after, or 4 hours in total. Plots are stereographic projections where each latitude circle is 10° separate from its neighbours and the innermost circle represents the 80° latitude band. Lower absolute values indicate lower potential vorticity, and vice-versa.

distribution set using a diurnally-averaged MY 34 CDOD map (Montabone et al., 2020). They show a daytime circulation that transports air to the SP, and a nighttime circulation that transports air away from it, exhibiting diurnal tidal variations and explaining the presence of dust and warmer air (expressed as lower absolute PV) on the SP dayside.

The MMC at different local times was calculated for MYs 33 and 34 (Fig. S2), to see if the described pattern holds under non-GDS conditions. The MY 34 results show very good agreement with Kleinböhl et al. (2020): a strong nighttime circulation away from the SP (MUTs 02:00, 22:00), a strong daytime circulation towards the SP (MUTs 10:00, 14:00), and a weaker dawn/dusk transitional circulation towards the SP (MUTs 06:00, 18:00). This day-night pattern also agrees well with the MY 34 EMARS reanalysis, which shows a boosted daytime poleward circulation and nighttime equatorward circulation early during the GDS (Gillespie et al., 2020). The presence of a (weak) circulation towards the SP at dawn/dusk explains why the PV minimum covers a small longitudinal extent. The MY 33 circulation closely resembles MY 34, but weaker. One would therefore expect a similar effect in MY 33: a higher absolute PV air mass, and a CDOD minimum, following Mars' nightside. The distinctive annular shape of the vortex is maintained throughout, including the central eye location around 80° S,-60° E (Fig. 6). However, there is also definite diurnal variation in PV and CDOD, with a localised increase in absolute PV following the nightside. The magnitude of this increase is highly longitudinally asymmetric: the PV minimum is over 3 MPVU greater at midnight at longitude 0° (Fig. 6.a) than longitude 180° (Fig. 6.d), likely due to stationary wave influence. There also appears to be a CDOD minimum following MUT ∼06:00 (Fig. 6.b,d,e,f). These results corroborate the Kleinböhl et al. (2020) finding that the observed MY 34 SP vortex behaviour is due to an enhanced MMC boosting an already present mechanism by which warmer, dustier air is transported to the dayside of the pole and colder, clearer air remains on the nightside. As well as the local time effect, there is also a complex interplay with southern stationary waves.

Finally, given the weaker northern circulation at this season one would expect a similar but weaker diurnal cycle at the NP vortex. Fig. S3 shows some diurnal variation in the PV maximum's longitude, roughly following the nightside, but it is less clear than in the south, and more dominated by apparent intrinsic longitudinal asymmetries. PV is consistently high, up to 50 MPVU, around longitudes -60-0° E for half the diurnal cycle, and around longitudes 150- -150° E for the other half; elsewhere, it is notably weaker even during local nighttime (e.g. MUT 02:00). This pattern is consistent with the observed residually elliptical PV structure visible in the diurnally averaged plot (Fig. 1.c). There is also an apparent minimum in CDOD diurnal variation following the PV maximum, as at the SP. Again, the pattern is less obvious than in the south. These results suggest local time variations at the NP similar to those in the SP, but largely obscured by planetary wave effects.

4 Discussion

The MY 34 GDS had a significant effect on the morphology of both the southern and northern polar vortices, through both altered dynamics (in the north) and a combination of altered dynamics and altered radiative heating (in the south). For both hemispheres, the change in the dynamics came in the form of changes to the meridional flow, linked to changes to the high latitude stationary wave structure. This stationary wave structure is an alternative interpretation of the morphology of both polar vortices at this time of year, with the northern wavenumber 2 feature following the NP vortex's characteristic elliptical shape. These are two possible perspectives, wave-based or PV-based, on the same phenomenon.

The GDS-induced changes to the stationary waves were reflected in changes in the shape of polar vortices, specifically reducing their longitudinal and, in the southern case, latitudinal asymmetry. Indeed, the amplitude changes in the northern hemisphere wavenumber 1 feature exactly correlate to modelled changes in PV. In the south, the GDS-induced changes to the heating rates in the atmosphere also had a crucial effect on the diurnally-averaged polar vortex structure. Increased atmospheric heating from the high southern dust loading in conjunction with dynamical heating reduced the meridional temperature gradient, substantially reducing the strength of the polar jet and causing large-scale PV mixing and dilution along the isentropic surface. The remnant westerly jet was shifted to a tighter area circumscribing the pole. This was a dramatic acceleration of the already ongoing decay of the SP vortex. In the north, by contrast, there were minimal changes in radiative heating rates at high latitudes, preserving the strength of the polar vortex even as its area and ellipticity decreased by the (longitudinally asymmetric) expansion of the Hadley cell to higher latitudes.

The effect of the GDS on northern stationary wave activity was twofold. Most relevant for the polar vortex, one effect was to shift the latitude of the NP jet northwards, away from the high amplitude zonal topography of the northern mid-latitudes which mechanically forces the wavenumber 2 stationary wave (Nayvelt et al., 1997), thereby reducing high latitude stationary wave activity associated with the polar jet. There was residual ellipticity in the MY 34 NP vortex, visible in the zonal wind and PV structure in Fig. 1.c and in remnant stationary wave activity between -90° E and 60° E, which can be likely attributed to the presence of high-latitude topographic gradients north of Alba Patera and in Acidalia Planitia. Secondly at lower, sub-45° N latitudes, where differential heating due to zonal topographic gradients plays a greater role in driving stationary wave activity (Nayvelt et al., 1997), the high dust loading of the GDS dramatically reduced zonal surface temperature gradients (Streeter, Lewis, Patel, Holmes, & Kass, 2020), thereby dramatically reducing stationary wave activity across all longitudes. This latter effect was less relevant for the high-latitude polar vortex. At southern high-latitudes, the already weak (relative to the north) stationary wave activity was substantially reduced as well. South of 60° S, where the dust cloud extended, the reduced meridional thermal gradient reduced zonal wind speeds, decreasing mechanical forcing and the wavenumber 1 stationary wave.

The stationary wave interpretation explains not only the elliptical polar vortex shape, but why the elliptical shape is more prevalent in the northern hemisphere, as noted by Waugh et al. (2016). The non-GDS northern hemisphere has, at the L_S=200-220° period, a strong and latitudinally extended wavenumber 2 feature. The southern hemisphere, by contrast, has a more ambiguous stationary wave structure at this time, with a mid-high latitude wavenumber 2 feature transitioning to a wavenumber 1 feature near the pole. These wave features most likely have a topographically-induced origin, both through mechanical forcing and differential heating (e.g. Nayvelt et al., 1997; Hollingsworth & Barnes, 1996; Haberle et al., 2019). Mitchell et al. (2015) and Rostami et al. (2018) hypothesised that the elliptical polar vortex shape might be linked to large-scale topography; here we provide compelling evidence that the elliptical shape of the vortices is the shape of the stationary planetary waves, by showing that the suppression of one entails the suppression of the other.

There was some apparent disagreement with previous literature on the effects of high dust loading on polar vortex structure, though this may be due to the time of year under consideration, among other factors. Mitchell et al. (2015), using the MACDA reanalysis, found that a regional-scale dust storm at L_S=320° caused a ∼10° latitude shift in the NP vortex, as well as an overall weakening in PV. This study shows little change in the broad morphology of the NP vortex even from the very high dust loading of a GDS, and only a localised weakening in PV. A couple of factors could be responsible for this disagreement. First, and likely most importantly, the times of year are different. At L_S=320°,

the NP vortex is already weakening as the planet approaches equinox, while in the L_S=200-220° period the NP vortex is strengthening as the planet approaches northern winter solstice. While a proper intercomparison between this reanalysis and MACDA is called for, this suggests that seasonal differences could be crucial in determining polar vortex response to sudden high dust loadings. The second factor is the nature of the regional storm in question itself, and specifically its spatial location. This could have an impact on its resultant dynamical and radiative effects.

Guzewich et al. (2014) investigated the impact of the MY 25 GDS on stationary waves, primarily the wavenumber 1 mode, finding that this mode was enhanced at both northern and southern high latitudes. The results presented here are consistent with Guzewich et al. (2014) for the northern hemisphere, as they show a marked decrease in amplitude of the wavenumber 2 mode and a transition towards a more apparently dominant wavenumber 1 mode; this is even more marked at higher altitudes than those shown here. The picture in the southern hemisphere is more complex however, as these results show decreased wavenumber 1 activity, even higher than 20-30 km (not shown). This is puzzling due to the close similarity in season and general structure between the MY 25 and MY 34 GDS, and further study is required to explain this difference.

Guzewich et al. (2016) found that the NP vortex was significantly disrupted in an MGCM with a prescribed high-dust peak at L_S=270°, but not with a dust peak of standard magnitude at L_S=200°. Reversing the seasonal dust loading did not impact the SP vortex. In the study presented here, the SP vortex was disproportionately affected by an equinoctial/early perihelion season GDS, when the NP/SP vortices are strengthening/weakening, respectively. This is not inconsistent with Guzewich et al. (2016), as they investigated the effects of high dust loading at southern summer solstice, L_S=270°, and standard dust loading at other times of year. Comparing the two sets of results suggests a key role for seasonality of high dust loading in resultant polar vortex behaviour. Given that GDS have been observed to occur at various times within the dusty season L_S=180-360° (Shirley, 2015), with the three most recent events occuring at equinox (MY 25), solstice (MY 28), and equinox (MY 34), it is worth investigating both equinoctial and solsticial events and the likely significant effect of GDS seasonality.

At this point it should be noted that despite the evidence of wave-related effects on the SP vortex structure, wave structure alone is not the whole story in explaining its broad morphology. Notably, planetary wave structure does not explain the off-pole presence of the eye of lower absolute PV. Following the hypothesis that the central absolute PV minimum is the result of localised diabatic heating from latent heat release as CO_2 condensation occurs over the pole (Toigo et al., 2017; Rostami et al., 2018), one would expect that this location in the reanalysis - approximately 80° S, -60° E - undergoes greater CO_2 condensation than the surrounding seasonal cap. The reanalysis and the MCS surface CO_2 ice observations from Piqueux et al. (2015) offer an opportunity to try to further validate this hypothesis. MCS observations from this period show a clear ice remnant present between 70-90° S and -120-60° E, even as the ice in the opposite hemisphere has almost completely disappeared (Piqueux et al., 2015). While the reanalysis shows a greater latitudinal extent of CO_2 ice coverage than the observations, it does agree with the observations regarding where the most CO_2 ice mass is located, at the same latitude range noted earlier. The location of this remnant surface ice feature agrees very well with the location of the low absolute PV eye seen in for example Fig. 1.b.

MCS observations suggest that this location is indeed an area of greater CO_2 condensation, resulting in a thicker and therefore longer lasting ice cap; alternatively, it could be that this region is colder than the surrounding areas, thereby promoting greater CO_2 condensation and less rapid sublimation. These "cold spots" could also be linked to the presence of CO_2 ice clouds (Hayne et al., 2012), and are an ongoing area of study. In any case, this would seem to be further supporting evidence for the Toigo et al. (2017) hypothesis for the cause of the annular PV structure. However, Figure 6 appears to show

that the local PV minimum or "eye" has lower absolute PV during local daytime. This is contrary to what might be expected if CO_2 condensation was the driving mechanism behind the eye, as condensation would be expected to occur preferentially at local night due to lower atmospheric temperatures. Indeed despite low local radiative flux, the interconnectedness of the global thermal tide can still force large diurnal atmospheric variations even at high latitudes (Lee et al., 2009). One way to account for this would be to consider the diurnal pattern of mass transport (Figure S2); air mass is transported towards the south pole during the daytime, thereby supplying more mass for condensation onto the seasonal cap. This may outweigh diurnal changes in radiative flux and atmospheric temperature causing sublimation/condensation, which will be low at such high latitudes. This remains to be investigated in future work. Finally, it is interesting to note that the GDS appears to shift the local PV minimum towards the pole itself, at least for the L_S=200-220° period; this shows that the GDS affects whatever mechanisms are responsible for location of the off-pole eye in non-GDS conditions.

Lastly, analysis of local time variations in the SP vortex during the GDS reproduce the Kleinböhl et al. (2020) results of an isolated (high absolute PV), dust-clear air mass trapped on the nightside. This study provides further evidence that the proposed mechanism, a boosting of the meridional circulation in MY 34 intensifying an existing local time pattern of nightside transport away from the SP and dayside transport towards, is indeed correct. This pattern is shown to exist at the same time period in MY 33, with a weaker but still visible impact on the diurnal variation of PV and CDOD. The weaker meridional circulation and stronger stationary wave activity means that the diurnally-averaged structure, consisting of an off-pole eye of lower absolute PV with a surrounding annulus of higher PV, remains visible at all local times. There is some diurnal variation in PV at the NP in MY 34, but this is much weaker than in the south.

5 Conclusions

The GDS had a significant impact on both the northern and southern polar vortices. In the north, the polar vortex structure (reflected via PV and zonal wind speeds) became less elliptical and more longitudinally symmetric. PV increased slightly at the pole itself and decreased at lower latitudes, indicating a narrowing of the area of the polar vortex as the Hadley cell descending branch extended further poleward. In the south, there was significant mixing and therefore local reduction of PV across the entire polar vortex, and a corresponding increase in near-pole wind speeds and decrease in wind speeds at lower latitudes. The remaining diurnally-averaged polar vortex was significantly more symmetric than in the non-GDS case, and centred at the pole itself rather than off-pole. The non-GDS asymmetries in polar vortex shape at both poles were found to be linked to a longitudinally asymmetric meridional flow, reflected in the stationary planetary wave structure in each hemisphere. The GDS significantly reduced the amplitude of the northern wavenumber 1 feature and almost entirely destroyed the southern stationary wave feature, which was expressed in more symmetrical polar vortices.

The MY 34 GDS also caused a peculiar feature at the southern pole: a mass of colder, isolated air coupled with a minimum in dust which followed the nightside of the planet, first seen in direct MCS observations (Kleinböhl et al., 2020). This feature was clearly visible in the reanalysis and its suggested causal mechanism, a boosted mean meridional circulation enhancing a pre-existing (non-GDS) pattern of nighttime air transport away from the southern pole and daytime air transport towards it, further corroborated. This pattern was shown to be present at the northern pole in a weaker form, and at the southern pole, albeit in a weaker form, in the non-GDS year MY 33.

The intensity and shape of the polar vortices and their corresponding westerly zonal jets control what can be transported above and onto the poles themselves. The non-GDS shape and GDS-induced alteration of the vortices therefore has potentially important

consequences for both seasonal and long-term transport of dust, water, and chemical species into the polar regions and onto the seasonal CO_2 caps. The substantially diminished diurnally-averaged southern vortex during an equinoctial GDS should provide a weaker barrier to transport into the southern polar region and onto the surface, while the relatively robust northern vortex should remain an effective barrier to transport. This is especially relevant considering the boosted meridional circulation during GDS. Additionally, if the poleward shift of the westerly jets is a consistent effect of equinoctial GDS, this implies that quantities such as dust, water, and chemical species can be transported to higher latitudes during these intense dust events. If this kind of pattern holds over the course of the thousands of years that Mars maintains its particular axial obliquity, this has further implications for the record of deposited dust at the southern and northern polar layered deposits, for example as measured by the SHARAD subsurface radar (Seu et al., 2018). Over long timescales, the spatially anchored morphology of the polar vortices may influence the longitudinal pattern of dust deposition over the polar regions.

Validation is an important consideration for results from a meteorological reanalysis, particularly when based on fields (PV, wind speeds) not directly measured from orbit. The most valuable possible future measurements would be of atmospheric winds from an orbiter. These would allow better constraints on the structure of the polar vortices, and (combined with temperature measurements) direct calculation of PV. In the near future, ongoing retrievals of temperature, dust, and long-lived trace gases from TGO and its NOMAD (Vandaele et al., 2015; Patel et al., 2017) and ACS (O. I. Korablev et al., 2015; O. Korablev et al., 2018) spectrometer suites will enable further investigation of tracer transport and an opportunity to cross-validate and jointly assimilate multiple orbiter observations. NOMAD/ACS provide the crucial feature of observing over a range of martian local times, enabling exploration of the diurnal cycles of tracer transport and polar dynamics.

Acknowledgments

PMS acknowledges support from the STFC under Grant ST/N50421X/1 and The Open University for a PhD studentship, and support from UKSA under grant ST/P005332/1. SRL, MRP, and JAH thank UKSA for support under grants ST/R001405/1, ST/P005332/1, ST/V00225/1, and ST/S00145X/1. AF acknowledges the Ministry of Science and Higher Education of the Russian Federation. AK acknowledges support from NASA's Mars Data Analysis program (NNN13D465T). Work at the Jet Propulsion Laboratory, California Institute of Technology, is performed under contract with the National Aeronautics and Space Administration. The authors are particularly grateful for ongoing collaborations with the MCS team (NASA-JPL), Peter Read (Oxford), and François Forget and colleagues (LMD/CNRS Paris). Scientific colour maps are from Crameri (2020). CODMAC Level 2 ACS data are available on the ESA PSA at `https://archives.esac.esa.int/psa/#!TableView/ACS=instrument`; see Fedorova et al. (2020) for details on the retrieval technique. CODMAC Level 5 MCS retrievals (v5) are publicly available on NASA's PDS at `https://atmos.nmsu.edu/data_and_services/atmospheres_data/MARS/mcs.html`. Reanalysis data used in this article are publicly available on the ORDO repository (Streeter, Lewis, Patel, & Holmes, 2020). The authors thank the Editor and two anonymous reviewers for their constructive comments which have helped to improve this manuscript.

References

Andrews, D. G., Holton, J. R., & Leovy, C. B. (1987). *Middle atmosphere dynamics.* Retrieved 2017-11-03, from `http://adsabs.harvard.edu/abs/1987mad..book.....A`

Barnes, J. R., & Haberle, R. M. (1996, November). The Martian Zonal-Mean Circulation: Angular Momentum and Potential Vorticity Structure in GCM Simulations. *Journal of the Atmospheric Sciences*, *53*(21), 3143–3156.

Retrieved 2019-01-25, from https://journals.ametsoc.org/doi/abs/10.1175/1520-0469(1996)053%3C3143%3ATMZMCA%3E2.0.CO%3B2 doi: 10.1175/1520-0469(1996)053⟨3143:TMZMCA⟩2.0.CO;2

Barnes, J. R., Pollack, J. B., Haberle, R. M., Leovy, C. B., Zurek, R. W., Lee, H., & Schaeffer, J. (1993, February). Mars atmospheric dynamics as simulated by the NASA AMES General Circulation Model. II - Transient baroclinic eddies. *Journal of Geophysical Research*, *98*, 3125–3148. Retrieved 2017-03-28, from http://adsabs.harvard.edu/abs/1993JGR....98.3125B doi: 10.1029/92JE02935

Crameri, F. (2020, January). *Scientific colour maps.* Zenodo. Retrieved 2020-11-10, from https://zenodo.org/record/4153113#.X6qN32j7SUl (Language: eng) doi: 10.5281/zenodo.4153113

Fedorova, A. A., Montmessin, F., Korablev, O., Luginin, M., Trokhimovskiy, A., Belyaev, D. A., ... Wilson, C. F. (2020, January). Stormy water on Mars: The distribution and saturation of atmospheric water during the dusty season. *Science*, *367*(6475), 297–300. Retrieved 2020-04-19, from https://science.sciencemag.org/content/367/6475/297 (Publisher: American Association for the Advancement of Science Section: Report) doi: 10.1126/science.aay9522

Forget, F., Hourdin, F., Fournier, R., Hourdin, C., Talagrand, O., Collins, M., ... Huot, J.-P. (1999, October). Improved general circulation models of the Martian atmosphere from the surface to above 80 km. *Journal of Geophysical Research: Planets*, *104*(E10), 24155–24175. Retrieved 2017-03-08, from http://onlinelibrary.wiley.com/doi/10.1029/1999JE001025/abstract doi: 10.1029/1999JE001025

Gillespie, H. E., Greybush, S. J., & Wilson, R. J. (2020). An Investigation of the Encirclement of Mars by Dust in the 2018 Global Dust Storm Using EMARS. *Journal of Geophysical Research: Planets*, *125*(7), e2019JE006106. Retrieved 2021-02-10, from https://agupubs.onlinelibrary.wiley.com/doi/abs/10.1029/2019JE006106 (_eprint: https://agupubs.onlinelibrary.wiley.com/doi/pdf/10.1029/2019JE006106) doi: https://doi.org/10.1029/2019JE006106

Guzewich, S. D., Toigo, A. D., & Waugh, D. W. (2016, November). The effect of dust on the martian polar vortices. *Icarus*, *278*(Supplement C), 100–118. Retrieved 2017-09-29, from http://www.sciencedirect.com/science/article/pii/S0019103516302846 doi: 10.1016/j.icarus.2016.06.009

Guzewich, S. D., Wilson, R. J., McConnochie, T. H., Toigo, A. D., Banfield, D. J., & Smith, M. D. (2014, March). Thermal tides during the 2001 Martian global-scale dust storm. *Journal of Geophysical Research: Planets*, *119*(3), 2013JE004502. Retrieved 2017-03-08, from http://onlinelibrary.wiley.com/doi/10.1002/2013JE004502/abstract doi: 10.1002/2013JE004502

Haberle, R. M., Kahre, M. A., Barnes, J. R., Hollingsworth, J. L., & Wolff, M. J. (2019, July). MARCI observations of a wavenumber-2 large-scale feature in the north polar hood of Mars: Interpretation with the NASA/Ames Legacy Global Climate Model. *Icarus*. Retrieved 2019-07-10, from http://www.sciencedirect.com/science/article/pii/S0019103519303057 doi: 10.1016/j.icarus.2019.07.001

Hayne, P. O., Paige, D. A., Schofield, J. T., Kass, D. M., Kleinböhl, A., Heavens, N. G., & McCleese, D. J. (2012). Carbon dioxide snow clouds on Mars: South polar winter observations by the Mars Climate Sounder. *Journal of Geophysical Research: Planets*, *117*(E8). Retrieved 2020-03-27, from https://agupubs.onlinelibrary.wiley.com/doi/abs/10.1029/2011JE004040 doi: 10.1029/2011JE004040

Haynes, P. H., & McIntyre, M. E. (1987, March). On the Evolution of Vorticity and Potential Vorticity in the Presence of Diabatic Heating and Frictional

or Other Forces. *Journal of the Atmospheric Sciences*, *44*(5), 828–841. Retrieved 2020-09-10, from https://journals.ametsoc.org/jas/article/44/5/828/22015/On-the-Evolution-of-Vorticity-and-Potential (Publisher: American Meteorological Society) doi: 10.1175/1520-0469(1987)044⟨0828:OTEOVA⟩2.0.CO;2

Hollingsworth, J. L., & Barnes, J. R. (1996, February). Forced stationary planetary waves in Mars's winter atmosphere. *Journal of Atmospheric Sciences*, *53*, 428–448. Retrieved 2017-03-09, from http://ukads.nottingham.ac.uk/abs/1996JAtS...53..428H doi: 10.1175/1520-0469(1996)053⟨0428:FSPWIM⟩2.0.CO;2

Holmes, J., Lewis, S., & Patel, M. (2019, February). *OpenMARS MY28-32 standard database* [Fileset]. Retrieved 2019-03-29, from https://ordo.open.ac.uk/articles/OpenMARS_MY28-32_standard_database/7352579

Holmes, J. A., Lewis, S. R., & Patel, M. R. (2017, January). On the link between martian total ozone and potential vorticity. *Icarus*, *282*, 104–117. Retrieved 2019-12-18, from http://www.sciencedirect.com/science/article/pii/S0019103516306510 doi: 10.1016/j.icarus.2016.10.004

Holmes, J. A., Lewis, S. R., Patel, M. R., & Lefèvre, F. (2018, March). A reanalysis of ozone on Mars from assimilation of SPICAM observations. *Icarus*, *302*, 308–318. Retrieved 2018-02-07, from http://www.sciencedirect.com/science/article/pii/S0019103517302889 doi: 10.1016/j.icarus.2017.11.026

Holmes, J. A., Lewis, S. R., Patel, M. R., & Smith, M. D. (2019, August). Global analysis and forecasts of carbon monoxide on Mars. *Icarus*, *328*, 232–245. Retrieved 2019-04-09, from http://www.sciencedirect.com/science/article/pii/S001910351830664X doi: 10.1016/j.icarus.2019.03.016

Hoskins, B. J., McIntyre, M. E., & Robertson, A. W. (1985). On the use and significance of isentropic potential vorticity maps. *Quarterly Journal of the Royal Meteorological Society*, *111*(470), 877–946. Retrieved 2020-09-10, from https://rmets.onlinelibrary.wiley.com/doi/abs/10.1002/qj.49711147002%4010.1002/%28ISSN%291477-870X.TheBrianHoskinsSpecialCollection (_eprint: https://rmets.onlinelibrary.wiley.com/doi/pdf/10.1002/qj.49711147002) doi: 10.1002/qj.49711147002

Kass, D. M., Kleinböhl, A., McCleese, D. J., Schofield, J. T., & Smith, M. D. (2016, June). Interannual similarity in the Martian atmosphere during the dust storm season. *Geophysical Research Letters*, *43*(12), 2016GL068978. Retrieved 2017-03-09, from http://onlinelibrary.wiley.com/doi/10.1002/2016GL068978/abstract doi: 10.1002/2016GL068978

Kass, D. M., Schofield, J. T., Kleinböhl, A., McCleese, D. J., Heavens, N. G., Shirley, J. H., & Steele, L. J. (2019a). Mars Climate Sounder observation of Mars' 2018 global dust storm. *Geophysical Research Letters*, *n/a*(n/a). Retrieved 2020-04-03, from https://agupubs.onlinelibrary.wiley.com/doi/abs/10.1029/2019GL083931 doi: 10.1029/2019GL083931

Kass, D. M., Schofield, J. T., Kleinböhl, A., McCleese, D. J., Heavens, N. G., Shirley, J. H., & Steele, L. J. (2019b). Mars Climate Sounder observation of Mars' 2018 global dust storm. *Geophysical Research Letters*, *n/a*(n/a). Retrieved 2019-12-16, from https://agupubs.onlinelibrary.wiley.com/doi/abs/10.1029/2019GL083931 doi: 10.1029/2019GL083931

Kleinböhl, A., Friedson, A. J., & Schofield, J. T. (2017, January). Two-dimensional radiative transfer for the retrieval of limb emission measurements in the martian atmosphere. *Journal of Quantitative Spectroscopy and Radiative Transfer*, *187*, 511–522. Retrieved from http://www.sciencedirect.com/science/article/pii/S0022407316302667 doi: 10.1016/j.jqsrt.2016.07.009

Kleinböhl, A., Schofield, J. T., Abdou, W. A., Irwin, P. G. J., & de Kok, R. J. (2011, July). A single-scattering approximation for infrared radiative trans-

fer in limb geometry in the Martian atmosphere. *Journal of Quantitative Spectroscopy and Radiative Transfer*, *112*, 1568–1580. Retrieved 2017-09-20, from http://adsabs.harvard.edu/abs/2011JQSRT.112.1568K doi: 10.1016/j.jqsrt.2011.03.006

Kleinböhl, A., Schofield, J. T., Kass, D. M., Abdou, W. A., Backus, C. R., Sen, B., ... McCleese, D. J. (2009, October). Mars Climate Sounder limb profile retrieval of atmospheric temperature, pressure, and dust and water ice opacity. *Journal of Geophysical Research: Planets*, *114*(E10), E10006. Retrieved 2016-10-21, from http://onlinelibrary.wiley.com/doi/10.1029/2009JE003358/abstract doi: 10.1029/2009JE003358

Kleinböhl, A., Spiga, A., Kass, D. M., Shirley, J. H., Millour, E., Montabone, L., & Forget, F. (2020). Diurnal Variations of Dust During the 2018 Global Dust Storm Observed by the Mars Climate Sounder. *Journal of Geophysical Research: Planets*, *125*(1), e2019JE006115. Retrieved 2020-03-25, from https://agupubs.onlinelibrary.wiley.com/doi/abs/10.1029/2019JE006115 doi: 10.1029/2019JE006115

Korablev, O., Montmessin, F., Trokhimovskiy, A., Fedorova, A. A., Shakun, A. V., Grigoriev, A. V., ... Zorzano, M. P. (2018). The Atmospheric Chemistry Suite (ACS) of Three Spectrometers for the ExoMars 2016 Trace Gas Orbiter. *Space Science Reviews*, *214*(1), 7. Retrieved 2020-11-03, from https://doi.org/10.1007/s11214-017-0437-6 doi: 10.1007/s11214-017-0437-6

Korablev, O. I., Montmessin, F., Fedorova, A. A., Ignatiev, N. I., Shakun, A. V., Trokhimovskiy, A. V., ... Kozlova, T. O. (2015, December). ACS experiment for atmospheric studies on "ExoMars-2016" Orbiter. *Solar System Research*, *49*(7), 529–537. Retrieved 2020-03-26, from https://doi.org/10.1134/S003809461507014X doi: 10.1134/S003809461507014X

Lee, C., Lawson, W. G., Richardson, M. I., Heavens, N. G., Kleinböhl, A., Banfield, D., ... Toigo, A. D. (2009, March). Thermal tides in the Martian middle atmosphere as seen by the Mars Climate Sounder. *Journal of Geophysical Research: Planets*, *114*(E3), E03005. Retrieved 2017-03-09, from http://onlinelibrary.wiley.com/doi/10.1029/2008JE003285/abstract doi: 10.1029/2008JE003285

Lewis, S. R., Collins, M., & Read, P. L. (1997, May). Data assimilation with a martian atmospheric GCM: an example using thermal data. *Advances in Space Research*, *19*, 1267–1270. Retrieved 2017-03-09, from http://adsabs.harvard.edu/abs/1997AdSpR..19.1267L doi: 10.1016/S0273-1177(97)00280-9

Lewis, S. R., Read, P. L., Conrath, B. J., Pearl, J. C., & Smith, M. D. (2007, December). Assimilation of thermal emission spectrometer atmospheric data during the Mars Global Surveyor aerobraking period. *Icarus*, *192*(2), 327–347. Retrieved 2017-03-09, from http://www.sciencedirect.com/science/article/pii/S0019103507003557 doi: 10.1016/j.icarus.2007.08.009

Lorenc, A. C., Bell, R. S., & Macpherson, B. (1991, January). The Meteorological Office analysis correction data assimilation scheme. *Quarterly Journal of the Royal Meteorological Society*, *117*(497), 59–89. Retrieved 2016-10-25, from http://onlinelibrary.wiley.com/doi/10.1002/qj.49711749704/abstract doi: 10.1002/qj.49711749704

Madeleine, J.-B., Forget, F., Millour, E., Montabone, L., & Wolff, M. J. (2011, November). Revisiting the radiative impact of dust on Mars using the LMD Global Climate Model. *Journal of Geophysical Research: Planets*, *116*(E11), E11010. Retrieved 2016-10-20, from http://onlinelibrary.wiley.com/doi/10.1029/2011JE003855/abstract doi: 10.1029/2011JE003855

McCleese, D. J., Kleinböhl, A., Kass, D. M., Schofield, J. T., Wilson, R. J., & Greybush, S. (2017, January). Comparisons of Observations and Simulations of the Mars Polar Atmosphere. In (p. 1104). Retrieved 2017-04-20, from http://adsabs.harvard.edu/abs/2017mamo.conf.1104M

McCleese, D. J., Schofield, J. T., Taylor, F. W., Calcutt, S. B., Foote, M. C., Kass, D. M., ... Zurek, R. W. (2007, May). Mars Climate Sounder: An investigation of thermal and water vapor structure, dust and condensate distributions in the atmosphere, and energy balance of the polar regions. *Journal of Geophysical Research: Planets*, *112*(E5), E05S06. Retrieved 2017-03-09, from http://onlinelibrary.wiley.com/doi/10.1029/2006JE002790/abstract doi: 10.1029/2006JE002790

McDunn, T., Bougher, S., Murphy, J., Kleinböhl, A., Forget, F., & Smith, M. (2013, February). Characterization of middle-atmosphere polar warming at Mars. *Journal of Geophysical Research: Planets*, *118*(2), 161–178. Retrieved 2017-11-03, from http://onlinelibrary.wiley.com/doi/10.1002/jgre.20016/abstract doi: 10.1002/jgre.20016

Mitchell, D. M., Montabone, L., Thomson, S., & Read, P. L. (2015, January). Polar vortices on Earth and Mars: A comparative study of the climatology and variability from reanalyses. *Quarterly Journal of the Royal Meteorological Society*, *141*(687), 550–562. Retrieved 2017-03-09, from http://onlinelibrary.wiley.com/doi/10.1002/qj.2376/abstract doi: 10.1002/qj.2376

Montabone, L., Forget, F., Millour, E., Wilson, R. J., Lewis, S. R., Cantor, B., ... Wolff, M. J. (2015, May). Eight-year climatology of dust optical depth on Mars. *Icarus*, *251*, 65–95. Retrieved 2016-10-19, from http://www.sciencedirect.com/science/article/pii/S0019103515000044 doi: 10.1016/j.icarus.2014.12.034

Montabone, L., Spiga, A., Kass, D. M., Kleinböhl, A., Forget, F., & Millour, E. (2020). Martian Year 34 Column Dust Climatology from Mars Climate Sounder Observations: Reconstructed Maps and Model Simulations. *Journal of Geophysical Research: Planets*, *n/a*(n/a), e2019JE006111. Retrieved 2020-03-25, from https://agupubs.onlinelibrary.wiley.com/doi/abs/10.1029/2019JE006111 doi: 10.1029/2019JE006111

Nayvelt, L., Gierasch, P. J., & Cook, K. H. (1997, April). Modeling and Observations of Martian Stationary Waves. *Journal of the Atmospheric Sciences*, *54*(8), 986–1013. Retrieved 2020-03-24, from https://journals.ametsoc.org/doi/full/10.1175/1520-0469%281997%29054%3C0986%3AMAOOMS%3E2.0.CO%3B2 doi: 10.1175/1520-0469(1997)054⟨0986:MAOOMS⟩2.0.CO;2

Patel, M. R., Antoine, P., Mason, J., Leese, M., Hathi, B., Stevens, A. H., ... Lopez-Moreno, J. J. (2017). NOMAD spectrometer on the ExoMars trace gas orbiter mission: part 2—design, manufacturing, and testing of the ultraviolet and visible channel. *Applied Optics*, *56*(10), 2771–2782. Retrieved 2017-04-05, from http://oro.open.ac.uk/49024/

Piqueux, S., Kleinböhl, A., Hayne, P. O., Kass, D. M., Schofield, J. T., & McCleese, D. J. (2015, May). Variability of the martian seasonal CO2 cap extent over eight Mars Years. *Icarus*, *251*, 164–180. Retrieved 2019-08-12, from http://www.sciencedirect.com/science/article/pii/S0019103514006022 doi: 10.1016/j.icarus.2014.10.045

Rostami, M., Zeitlin, V., & Montabone, L. (2018, November). On the role of spatially inhomogeneous diabatic effects upon the evolution of Mars' annular polar vortex. *Icarus*, *314*, 376–388. Retrieved 2018-07-10, from http://www.sciencedirect.com/science/article/pii/S0019103517306073 doi: 10.1016/j.icarus.2018.05.026

Salby, M. L. (2011). *Physics of the Atmosphere and Climate.* Retrieved from http://public.eblib.com/choice/publicfullrecord.aspx?p=807160

Scott, R. K., Seviour, W. J. M., & Waugh, D. W. (2020). Forcing of the Martian polar annulus by Hadley cell transport and latent heating. *Quarterly Journal of the Royal Meteorological Society*, *146*(730), 2174–2190. Retrieved 2021-01-21, from https://rmets.onlinelibrary.wiley.com/doi/abs/10.1002/qj.3786

(_eprint: https://rmets.onlinelibrary.wiley.com/doi/pdf/10.1002/qj.3786) doi: https://doi.org/10.1002/qj.3786

Seu, R., Phillips, R. J., Biccari, D., Orosei, R., Masdea, A., Picardi, G., ... Nunes, D. C. (2018, February). SHARAD sounding radar on the Mars Reconnaissance Orbiter. *Journal of Geophysical Research: Planets*. Retrieved 2020-04-04, from https://agupubs.onlinelibrary.wiley.com/doi/full/10.1029/2006JE002745%4010.1002/%28ISSN%292169-9100.MARSROM1 doi: 10.1029/2006JE002745@10.1002/(ISSN)2169-9100.MARSROM1

Seviour, W. J. M., Waugh, D. W., & Scott, R. K. (2017, February). The Stability of Mars's Annular Polar Vortex. *Journal of the Atmospheric Sciences*, *74*(5), 1533–1547. Retrieved 2020-03-26, from https://journals.ametsoc.org/doi/full/10.1175/JAS-D-16-0293.1 doi: 10.1175/JAS-D-16-0293.1

Shirley, J. H. (2015, May). Solar System dynamics and global-scale dust storms on Mars. *Icarus*, *251*, 128–144. Retrieved 2017-03-09, from http://www.sciencedirect.com/science/article/pii/S0019103514005132 doi: 10.1016/j.icarus.2014.09.038

Smith, I. B., Diniega, S., Beaty, D. W., Thorsteinsson, T., Becerra, P., Bramson, A. M., ... Titus, T. N. (2017, June). 6th international conference on Mars polar science and exploration: Conference summary and five top questions. *Icarus*. Retrieved 2017-09-29, from http://www.sciencedirect.com/science/article/pii/S0019103517300465 doi: 10.1016/j.icarus.2017.06.027

Smith, M. D. (2004, January). Interannual variability in TES atmospheric observations of Mars during 1999–2003. *Icarus*, *167*(1), 148–165. Retrieved 2017-03-09, from http://www.sciencedirect.com/science/article/pii/S0019103503002872 doi: 10.1016/j.icarus.2003.09.010

Steele, L. J., Lewis, S. R., & Patel, M. R. (2014, July). The radiative impact of water ice clouds from a reanalysis of Mars Climate Sounder data. *Geophysical Research Letters*, *41*(13), 4471–4478. Retrieved 2017-03-09, from http://onlinelibrary.wiley.com/doi/10.1002/2014GL060235/abstract doi: 10.1002/2014GL060235

Streeter, P. M., Lewis, S. R., Patel, M. R., & Holmes, J. A. (2020, November). *Asymmetric impacts on Mars' polar vortices from an equinoctial Global Dust Storm.* (Publisher: The Open University type: dataset) doi: https://doi.org/10.21954/ou.rd.13218095.v2

Streeter, P. M., Lewis, S. R., Patel, M. R., Holmes, J. A., & Kass, D. M. (2020). Surface Warming During the 2018/Mars Year 34 Global Dust Storm. *Geophysical Research Letters*, *47*(9), e2019GL083936. Retrieved 2020-05-17, from https://agupubs.onlinelibrary.wiley.com/doi/abs/10.1029/2019GL083936 (_eprint: https://agupubs.onlinelibrary.wiley.com/doi/pdf/10.1029/2019GL083936) doi: 10.1029/2019GL083936

Toigo, A. D., Waugh, D. W., & Guzewich, S. D. (2017). What causes Mars' annular polar vortices? *Geophysical Research Letters*, *44*(1), 71–78. Retrieved 2019-09-03, from https://agupubs.onlinelibrary.wiley.com/doi/abs/10.1002/2016GL071857 doi: 10.1002/2016GL071857

Toon, O. B., McKay, C. P., Ackerman, T. P., & Santhanam, K. (1989). Rapid calculation of radiative heating rates and photodissociation rates in inhomogeneous multiple scattering atmospheres. *Journal of Geophysical Research: Atmospheres*, *94*(D13), 16287–16301. Retrieved 2019-08-12, from https://agupubs.onlinelibrary.wiley.com/doi/abs/10.1029/JD094iD13p16287 doi: 10.1029/JD094iD13p16287

Vandaele, A. C., Neefs, E., Drummond, R., Thomas, I. R., Daerden, F., Lopez-Moreno, J. J., ... Wolff, M. (2015, December). Science objectives and performances of NOMAD, a spectrometer suite for the ExoMars TGO mis-

sion. *Planetary and Space Science*, *119*, 233–249. Retrieved 2017-03-09, from http://www.sciencedirect.com/science/article/pii/S0032063315003025 doi: 10.1016/j.pss.2015.10.003

Waugh, D. W., Toigo, A. D., & Guzewich, S. D. (2019, January). Age of martian air: Time scales for martian atmospheric transport. *Icarus*, *317*, 148–157. Retrieved 2019-01-25, from http://www.sciencedirect.com/science/article/pii/S0019103518300034 doi: 10.1016/j.icarus.2018.08.002

Waugh, D. W., Toigo, A. D., Guzewich, S. D., Greybush, S. J., Wilson, R. J., & Montabone, L. (2016, September). Martian polar vortices: Comparison of reanalyses. *Journal of Geophysical Research: Planets*, *121*(9), 2016JE005093. Retrieved 2017-03-09, from http://onlinelibrary.wiley.com/doi/10.1002/2016JE005093/abstract doi: 10.1002/2016JE005093

Wilson, R. J. (1997, January). A general circulation model simulation of the Martian polar warming. *Geophysical Research Letters*, *24*(2), 123–126. Retrieved 2017-03-09, from http://onlinelibrary.wiley.com/doi/10.1029/96GL03814/abstract doi: 10.1029/96GL03814

Wolff, M. J., Lopéz-Valverde, M., Madeleine, J.-B., Wilson, R. J., Smith, M. D., Fouchet, T., & Delory, G. T. (2017, June). *Radiative Process: Techniques and Applications.* Retrieved 2019-08-23, from /core/books/atmosphere-and-climate-of-mars/radiative-process-techniques-and-applications/6EBC719A21887475E29CEAC6149C0D38 doi: 10.1017/9781139060172.006

Wolff, M. J., Smith, M. D., Clancy, R. T., Arvidson, R., Kahre, M., Seelos, F., ... Savijärvi, H. (2009, June). Wavelength dependence of dust aerosol single scattering albedo as observed by the Compact Reconnaissance Imaging Spectrometer. *Journal of Geophysical Research (Planets)*, *114*, E00D04. Retrieved 2017-04-12, from http://adsabs.harvard.edu/abs/2009JGRE..114.0D04W doi: 10.1029/2009JE003350

Wolff, M. J., Smith, M. D., Clancy, R. T., Spanovich, N., Whitney, B. A., Lemmon, M. T., ... Squyres, S. W. (2006). Constraints on dust aerosols from the Mars Exploration Rovers using MGS overflights and Mini-TES. *Journal of Geophysical Research: Planets*, *111*(E12), n/a–n/a. Retrieved from http://dx.doi.org/10.1029/2006JE002786 doi: 10.1029/2006JE002786

Zurek, R. W., & Smrekar, S. E. (2007). An overview of the Mars Reconnaissance Orbiter (MRO) science mission. *Journal of Geophysical Research: Planets*, *112*(E5). Retrieved 2020-11-03, from https://agupubs.onlinelibrary.wiley.com/doi/abs/10.1029/2006JE002701%4010.1002/%28ISSN%292169-9100.MARSROM1 (_eprint: https://agupubs.onlinelibrary.wiley.com/doi/pdf/10.1029/2006JE002701) doi: 10.1029/2006JE002701